



Pseudospectral methods for Boussinesq-type equations in an annular domain with applications to mid-sized lakes

D.T. Steinmoeller*, M. Stastna, K.G. Lamb

Department of Applied Mathematics, University of Waterloo, 200 University Ave. W., Waterloo, Ontario, Canada N2L 3G1

ARTICLE INFO

Article history:

Received 7 November 2011

Received in revised form 17 January 2012

Accepted 29 January 2012

Available online 7 February 2012

Keywords:

Shallow water

Pseudospectral methods

Physical limnology

Boussinesq equations

ABSTRACT

We present a numerical solution procedure for a two-dimensional Boussinesq-type shallow water model on annular domains using pseudospectral discretization methods, including practical implementation details such as spectral filtering to prevent aliasing-driven instabilities and efficient numerical linear algebra techniques. The numerical model's potential for predicting and simulating wave motions in mid-sized lakes is illustrated with three test cases: (1) wave diffraction around an island and near-shore focusing; (2) the formation, propagation and destruction of wave trains and solitary-like waves in rotating basins; and (3) the influence of bottom bathymetry on wave formation and propagation from a Kelvin-seiche.

© 2012 Elsevier B.V. All rights reserved.

1. Introduction

While the motion of fluids in the natural environment spans length scales from centimeters to thousands of kilometers, the majority of numerical models used in practical applications (weather prediction, pollution prediction and control) rely on the fact that naturally occurring fluids tend to be density stratified, and hence restrict motion to be predominantly horizontal, or in other words to occur in superimposed layers. Other factors, such as the Earth's rotation and the vertical thinness of the fluid layer relative to horizontal length scale, further contribute to making these naturally occurring flows dominated by horizontal motions. The numerical solution of layered models, though these are an approximation of the full equations of motions, thus forms an important class of applied numerical analysis problems. While the shallow water equations [1,2], the prototype of the layered model, are an example of a classical, nonlinear hyperbolic system, many natural physical extensions lie beyond the classical hyperbolic theory. Examples include models of wetting and drying [3], multi-layer models [4], sediment morphological models [5], and models that attempt to model the dispersive behaviour of naturally occurring waves [6,7].

Most mid-latitude lakes in the ice free seasons are primarily forced by the wind, which injects energy on large scales. These basin

scale motions are subsequently cascaded over a vast range of length scales, eventually leading to dissipation of the mechanical energy at the Kolmogorov length scale [8,9]. While some of the motions are quite irregular, many are coherent, with prominent examples being internal waves, Langmuir circulations and surface waves. The models considered in the following focus on internal waves in lakes which can occur on length scales ranging from kilometers to tens of meters.

The model equations under consideration here are the same as those used by de la Fuente et al. [6] in their study of the evolution of basin-scale Poincaré and Kelvin waves in a two-layer rotating basin using the finite volume method (FVM). The system of model equations represents a so-called Boussinesq-type system that is best described as an extension of the traditional shallow water equations to include weakly non-hydrostatic, i.e., dispersive, corrections to the hydrostatic pressure. Boussinesq-type models have previously been used to study dispersive and nonlinear effects in internal waves by Tomasson and Melville [10] and Brandt et al. [11]. The original concept of a Boussinesq-type model can be traced back to the approximation made by the model's name-sake, Boussinesq [1], in an effort to model solitary waves. An important consequence of using a Boussinesq-type model over the traditional shallow water model is that shocks, which are ubiquitous in classical nonlinear hyperbolic equation theory, are precluded by the dispersive nature of the short waves. The exclusion of shocks has significant implications in potential numerical methodologies, since shock-resolving methods [12,13] are no longer required to ensure numerical stability.

* Corresponding author.

E-mail address: dsteinmo@math.uwaterloo.ca (D.T. Steinmoeller).

The main contribution of this work is the use of high-order pseudospectral spatial discretization methods that are known to give the best accuracy possible and excellent resolution characteristics (see Boyd [14] or Trefethen [15]). Unlike the FVM that imparts inherent numerical dissipation to solutions [12], pseudospectral methods lack inherent dissipation, and the modeller must specify a small amount of artificial dissipation using either a hyperviscosity term or a spectral filter in order to stabilize the scheme [14,16].

Moreover, the methods developed in the following allow the numerical modelling of closed (albeit specialized) basins. While circular basins may seem to be an esoteric case, they form a well studied class of problems in physical limnology dating back over a century [17,18]. High order numerical methods for such basins allow the robustness of classical solutions to be explored without the uncertainty associated with the inherent dissipation in many low order methods. This, in turn, allows for a rational set of hypotheses to be formulated for subsequent testing against field data.

The remainder of the manuscript is organized as follows. First the methods, including the model equations, are presented in Section 2, including a description of the practical issues of implementation (including filtering and numerical linear algebra). This is followed by a presentation of model results (Section 3), subdivided into three categories: (1) wave diffraction around an island and near-shore wave focusing, (2) the formation, propagation and destruction of wave trains and solitary-like waves, and the effect of rotation, (3) the influence of bottom bathymetry on wave formation and propagation. Finally, in Section 4, conclusions drawn from our results are presented alongside a summary.

2. Methods

The governing equations used by de la Fuente et al. [6] in their study of internal waves in a circular basin for a single fluid layer are

$$\frac{\partial h}{\partial t} + \nabla \cdot (h\mathbf{u}) = 0, \quad (1)$$

$$\frac{\partial (uh)}{\partial t} + \nabla \cdot ((uh)\mathbf{u}) = -g'h \frac{\partial \eta}{\partial x} + fv_h + N_u, \quad (2)$$

$$N_u = \frac{H^2}{6} \frac{\partial}{\partial x} \left(\nabla \cdot \frac{\partial (uh)}{\partial t} \right), \quad (3)$$

$$\frac{\partial (vh)}{\partial t} + \nabla \cdot ((vh)\mathbf{u}) = -g'h \frac{\partial \eta}{\partial y} - fu_h + N_v, \quad (4)$$

$$N_v = \frac{H^2}{6} \frac{\partial}{\partial y} \left(\nabla \cdot \frac{\partial (vh)}{\partial t} \right), \quad (5)$$

where $\mathbf{u} = (u(x, y, t), v(x, y, t))$ is the velocity field, $h(x, y, t) = H(x, y) + \eta(x, y, t)$ is the total layer thickness with H representing the undisturbed layer thickness, and η is the interface displacement. Here we use the system (1)–(4) as a simple model of the baroclinic mode for a two-layer fluid with upper and lower layer densities of ρ_1 and ρ_2 , respectively. The constants $g' = g(\rho_2 - \rho_1)/\rho_2$ and f are reduced gravity and the Coriolis frequency, respectively. The difference between the set of equations (1)–(4) and the traditional shallow water model is the inclusion of the dispersive terms $(H^2/6) \nabla \cdot (\nabla \cdot (uh)_t)$ found in the momentum equations (2) and (4) and labeled N_u and N_v , respectively. The above system was first proposed by [11] in their study of internal waves in the Strait of Messina. This system is derived by a perturbation expansion in powers of the small dimensionless parameter $\mu = (H/L)$, and therefore is only physically accurate if $\mu \ll 1$.

In this study, we rewrite the system (1), (2) and (4) in non-conservative form and in standard polar coordinates $(r, \theta) \in [r_{\min}, r_{\max}] \times [0, 2\pi]$. The mixed space/time derivatives are

removed from the system by introducing the auxiliary scalar variable $z = \nabla \cdot \mathbf{u}_t$ and deriving an elliptic equation for z by taking the divergence of the momentum equations, as was done by Eskilsson and Sherwin [19] who solved a similar system of equations with the discontinuous Galerkin finite element method (DG-FEM). The main benefit of this approach over simply applying the same time-discretization scheme to all the time-derivatives is that it reduces the dimension of the resulting linear system to be solved at each time-step by a factor of two [19]. The resulting augmented system is

$$\frac{\partial h}{\partial t} + \frac{1}{r} \left(\frac{\partial (rhu_r)}{\partial r} + \frac{\partial (hu_\theta)}{\partial \theta} \right) = 0, \quad (6)$$

$$\frac{\partial u_r}{\partial t} = a_r + \gamma \frac{\partial z}{\partial r}, \quad (7)$$

$$\frac{\partial u_\theta}{\partial t} = a_\theta + \gamma \frac{\partial z}{\partial \theta}, \quad (8)$$

$$\nabla \gamma \cdot \nabla z + \gamma \nabla^2 z = \nabla \cdot \mathbf{a}, \quad (9)$$

with

$$\nabla = r \frac{\partial}{\partial r} + \hat{\theta} \frac{1}{r} \frac{\partial}{\partial \theta}, \quad (10)$$

$$\nabla^2 = \frac{1}{r} \frac{\partial}{\partial r} r \frac{\partial}{\partial r} + \frac{1}{r^2} \frac{\partial^2}{\partial \theta^2}, \quad (11)$$

$$\nabla \cdot \mathbf{a} = \frac{1}{r} \left(\frac{\partial (ra_r)}{\partial r} + \frac{\partial a_\theta}{\partial \theta} \right), \quad (12)$$

$$\mathbf{a} = a_r \hat{r} + a_\theta \hat{\theta}, \quad (13)$$

we find that

$$a_r = -u_r \frac{\partial u_r}{\partial r} - \frac{u_\theta}{r} \frac{\partial u_r}{\partial \theta} + \frac{u_\theta^2}{r} - g' \frac{\partial \eta}{\partial r} + fu_\theta, \quad (14)$$

$$a_\theta = -\frac{g'}{r} \frac{\partial \eta}{\partial \theta} - fu_r - u_r \frac{\partial u_\theta}{\partial r} - \frac{u_\theta}{r} \frac{\partial u_\theta}{\partial \theta} - \frac{u_r u_\theta}{r}, \quad (15)$$

where $\gamma = H^2/6$ is, in general, allowed to vary in space, and u_r and u_θ are the radial and annular velocities, respectively. In moving from the system (1)–(5) to (7)–(9), we have invoked the *mild slope* approximation $\nabla h \approx 0$ in the non-hydrostatic term, so that

$$\gamma \nabla \cdot (\nabla \cdot (uh)_t) \approx \gamma h \nabla \cdot (\nabla \cdot \mathbf{u}_t). \quad (16)$$

Such approximations are common in Boussinesq-type models [6,11] where high accuracy modelling of short-wave/topography interactions is not of primary concern.

The system is discretized in space using a Fourier pseudospectral method in the annular direction and a Chebyshev pseudospectral method in the radial direction. In our simulations, we always take $r_{\min} > 0$ to avoid the singularity and undesired clustering of grid points near $r = 0$ that are associated with the standard polar coordinates mapping. It is worth mentioning, however, that it is possible to reduce the amount of undesired clustering of Chebyshev points near the origin by using a mapped Chebyshev grid that is only heavily clustered near the outer boundary, as explored by Boyd and Yu [20].

The boundary conditions imposed are reflective wall conditions at the inner and outer radii of the basin:

$$u_r = 0 \quad \text{at} \quad r = r_{\min}, r_{\max}, \quad (17)$$

$$\frac{\partial \eta}{\partial r} = 0 \quad \text{at} \quad r = r_{\min}, r_{\max}. \quad (18)$$

A suitable time-dependent inhomogenous Neuman boundary condition for the elliptic variable z is obtained by taking the dot-product between the vector form of the momentum equations (7)

and (8) and the unit outward boundary normal $\hat{\mathbf{n}}$ and solving for the normal derivative of z , i.e.,

$$\frac{\partial z}{\partial n} = -\frac{\mathbf{a} \cdot \hat{\mathbf{n}}}{\gamma} \quad \text{at } r = r_{\min}, r_{\max}, \quad (19)$$

where we have used the fact that $\mathbf{u} \cdot \hat{\mathbf{n}} = 0$ at $r = r_{\min}, r_{\max}$.

The main basis for the spatial discretization method used here is the so-called pseudospectral technique, described by Peyret [21]: differentiate in the spectral space (i.e., the space of the expansion coefficients), and perform products in physical space in a point-wise manner. A central difficulty that arises from this “point-wise product” approach is that it results in aliasing errors that, in turn, tend to drive weak numerical instabilities [13]. Even stronger numerical instabilities may be driven by regions of high gradient in the solution that form due to nonlinear steepening, and require some amount of artificial numerical diffusion to ‘smooth out’ the solution and retain numerical stability. To overcome these problems, we have employed a spatial cut-off filter (see discussion below).

For speed and memory efficiency, Fourier and Chebyshev differentiation are implemented with the Fast Fourier Transform (FFT). The elliptic problem (9) is solved iteratively with the generalized minimum residual method (GMRES) using the LU-factorization of the second-order central finite differences approximation [22] of the elliptic operator as a pre-conditioner in order to reduce the iteration count to a reasonable number. For a discussion of GMRES and pre-conditioning, see [23].

Once the spatial discretization has been addressed, the problem is reduced to solving a system of ordinary differential equations in time that must be discretized and stepped forward in time. This approach is often referred to as the *method of lines* [15]. The temporal discretization was carried out with the second-order accurate Leapfrog method. A spatial wavenumber cut-off filter, similar to that used by Hesthaven and Warburton [13] for the DG-FEM method, of the form

$$\sigma(k) = \begin{cases} 1, & 0 \leq k < k_{\text{crit}} \\ \exp\left(\alpha \left(\frac{k - k_{\text{crit}}}{k_{\text{max}} - k_{\text{crit}}}\right)^s\right), & k_{\text{crit}} \leq k \leq k_{\text{max}} \end{cases} \quad (20)$$

was used in both r and θ directions during time-stepping to prevent aliasing errors from driving weak numerical instabilities. Filtering was performed by multiplying the filter function $\sigma(k)$ by the spectral coefficients of each solution field (u, v, η) after each time-step. The spectral coefficients were obtained using the FFT in the annular direction and a discrete cosine transform (DCT) in the radial direction. The filtered solution fields were hence obtained using the appropriate inverse transform. The parameters $\alpha < 0$, s , and k_{crit} are tunable and, in general, their values must be determined through experimentation.

3. Results

3.1. Model parameters

In the results presented in this manuscript, the model resolution was given by $N_r = 256$ radial (Chebyshev) points and $N_\theta = 1024$ annular (equispaced, Fourier) points. The spatial filtering parameters were typically taken to be: $k_{\text{crit}} = 0.15k_{\text{max}}$, $s = 4$, $\alpha = \ln 10^{-12}$, where k_{max} is the Nyquist wavenumber.

The GMRES convergence criterion was chosen to require the relative residual to be smaller than 10^{-8} . The number of GMRES iterations required per time-step varied by simulation, but was typically between 9 and 16 and fluctuated throughout run-time. A sudden growth in iteration count during time-stepping tended to indicate that the simulation was approaching a numerical

instability, and thus that the model should be re-run with a different set of filtering parameters to ensure stability.

The time-step Δt was determined through experimentation, but the CFL condition was always employed as a first guess or “rule of thumb”:

$$\Delta t \leq \frac{\min_{(r,\theta)}\{\Delta r, r\Delta\theta\}}{U_{\text{max}} + \sqrt{g'H}}, \quad (21)$$

where $U_{\text{max}} = \max_{(r,\theta)} \sqrt{(u_{r,0})^2 + (u_{\theta,0})^2}$ is the maximum speed of the initial conditions.

The numerical methodology was validated against approximate analytical solutions in one dimension and compared to numerical solutions in two dimensions obtained with the DG-FEM method (not shown) at various orders of accuracy. The pseudospectral method presented here was found to have better resolution and energy-conserving characteristics than the DG-FEM method in all cases. In particular, many fine scale flow features found in the results shown below are not present in the low order DG-FEM simulations, likely because they are ‘smeared out’ by numerical diffusion.

3.2. Test Case I: wave diffraction around an island and near-shore focusing (hereafter, WDAINF)

In the first test case, the inner and outer basin radii were taken to be $r_{\min} = 100$ m and $r_{\max} = 1272$ m, respectively. The mean fluid depth was set to $H = 10$ m (constant), the reduced gravity was taken as $g' = 0.196 \text{ m s}^{-2}$, and rotation was turned off ($f = 0$). The initial conditions were taken to be

$$\eta_0 = e^{-0.5(y+600)^2}, \quad (22)$$

$$u_{\theta,0} = 0, \quad (23)$$

$$u_{r,0} = 0, \quad (24)$$

representing a still fluid with a rectangular Gaussian interface perturbation stretching across the west–east length of the basin centered about the line $y = -600$ m. Here, subscript ‘0’ denotes the respective flow variable at time $t = 0$.

Since the fluid is initially at rest, the initial condition splits into two component waves, one travelling northward and one travelling southward (see Fig. 1). At $t = 6.6$ min, the southward propagating wave begins to strengthen as it propagates longshore and approaches the southern end of the basin. Meanwhile, the northward propagating wave is diffracting around the circular island centered at $(x, y) = (0, 0)$. At $t = 13.3$ min, the initially northward propagating wave is beginning to focus as it approaches the northern end of the basin, while the initially southward propagating wave has reflected off the southern coastline and has begun propagating northward, now focused as a predominantly single egg-shaped elevation wave. The process continues for all other times shown, with the focused waves spreading and undergoing wave–wave interactions with waves propagating in the opposite direction.

3.3. Test Case II: the formation, propagation and destruction of wave trains and solitary-like waves, and the effect of rotation (hereafter, FPDWT)

In our next test case, the physical parameters were chosen such that the idealized circular basin would be similar to the physical situation of Lake Kinneret, Israel by inferring approximate values from the data presented in [24]. To that end, the physical parameters were chosen as follows: $r_{\max} = 8435$ m, $r_{\min} = 1$ km, $g' = 0.024525 \text{ m s}^{-2}$, $H = 12.8$ m, $f = 7.8828 \times 10^{-5} \text{ s}^{-1}$. Under these parameters, the

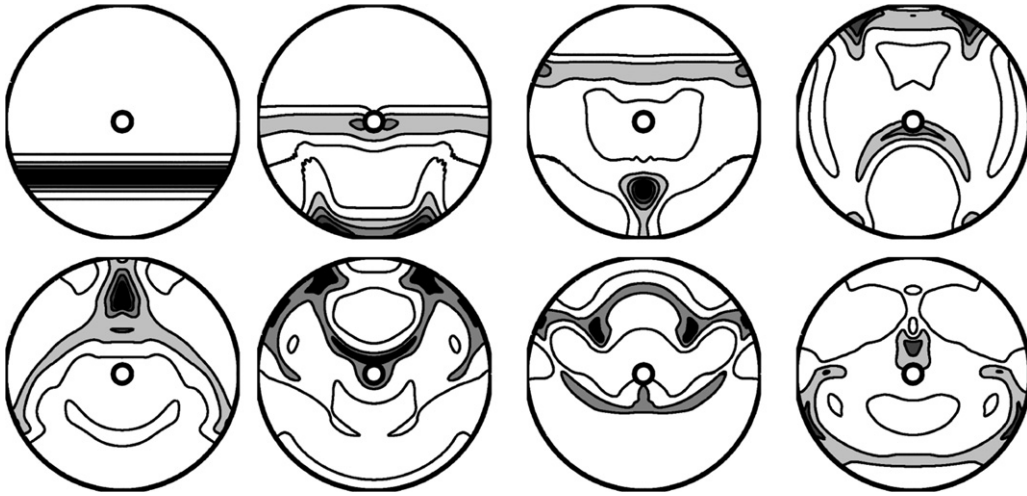


Fig. 1. Selected snapshots of the η field in the WDAINF test-case at times $t = 0, 6.6, 13.3, 19.7$ min (top) and $t = 26.2, 32.8, 39.4, 45.9$ min (bottom). The contour interval is given by five evenly spaced contours between $\eta = 0$ (white) and $\eta = \eta_0^{max} = 1$ (black). The inner and outer basin radii are given by $r_{min} = 100$ m and $r_{max} = 1272$ m, respectively. Rotation was turned off in this test-case ($f = 0$).

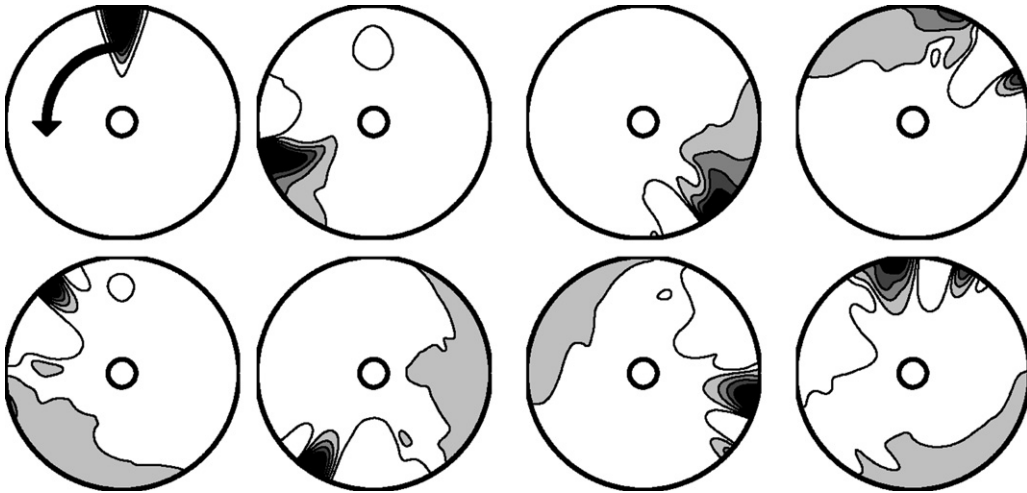


Fig. 2. Evolution of an initial interfacial perturbation propagating in the counter-clockwise longshore direction in the FPDWT test case with $f = 7.8828 \times 10^{-5} \text{ s}^{-1}$, $r_{min} = 1$ km, $r_{max} = 8345$ m. Snapshots were taken at $t = 0, 7, 14, 21$ h (top) and $t = 28, 35, 42, 49$ h (bottom). The maximum amplitude of the perturbation was taken to be $\eta_0^{max} = 0.01H$. The contour interval is given by five equally spaced values between $-0.03 \eta_0^{max}$ (white) and $0.375 \eta_0^{max}$ (black).

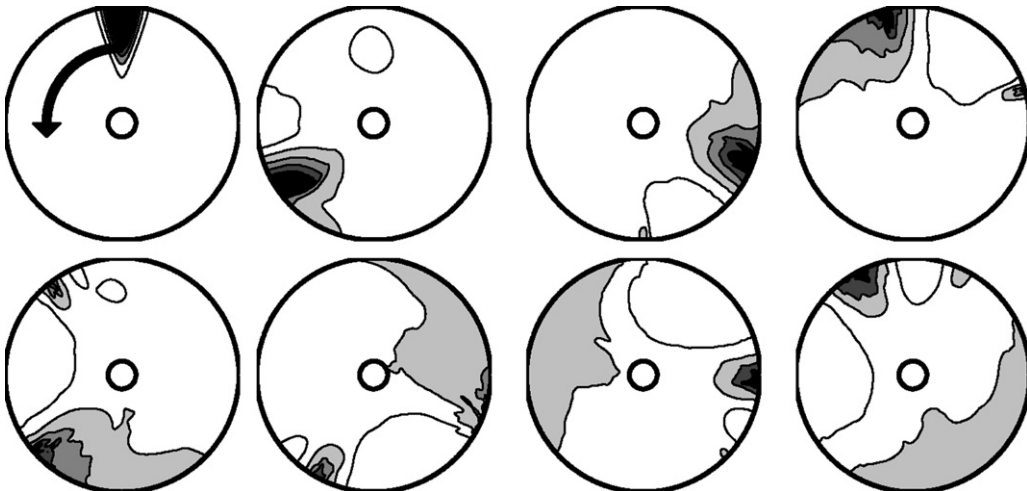


Fig. 3. Like Fig. 2, but with $\eta_0^{max} = 0.25H$.

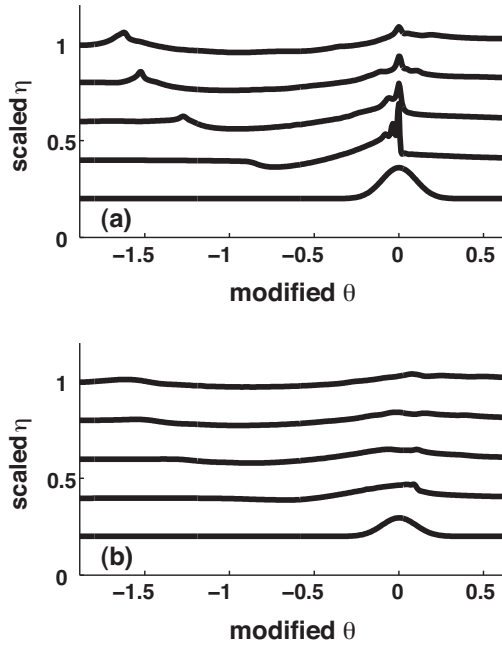


Fig. 4. 1D slices of the snapshots presented in Fig. 3 through the circles (a) $r = r_{\max} = 8435$ m and (b) $r = 2268$ m. In each panel, a single curve corresponds to a time in Fig. 3, with the lowest curve giving a slice through the initial condition ($t = 0$ h) and the uppermost curve giving a slice through the snapshot taken at $t = 28$ h. The slices have been shifted in such a way that the main wave-front is centered about $\theta = 0$, and η has been made dimensionless by dividing by the undisturbed layer thickness H .

Rossby deformation radius is $L_D = \sqrt{g'H}/f = 7107$ m, which is quite similar to the distance between the inner and outer basin radii.

The initial conditions are taken to be

$$\eta_0 = \eta_0^{\max} e^{-10^{-7}(r-r_{\max})^2 - 50(\theta - \frac{\pi}{2})^2}, \quad (25)$$

$$u_{\theta,0} = \sqrt{\frac{g'}{H}} \eta_0, \quad (26)$$

$$u_{r,0} = 0, \quad (27)$$

representing a coastally localized interfacial perturbation propagating in the annular direction at the long internal wave speed $\sqrt{g'H}$.

In Figs. 2 and 3 the maximum amplitude of the initial disturbance was taken to be $0.01H$ and $0.25H$, respectively to illustrate the effect of nonlinearity on a coastally-propagating wave in a lake similar to Lake Kinneret.

In Fig. 2, the effects of nonlinearity are negligible, and as a result no steepening occurs. By $t = 14$ h, the initial shape of the disturbance has spread out considerably and a region of interfacial depression follows the primary elevation wave. By $t = 28$ h, the region behind the depression has become the highest point of interfacial elevation, and the region of largest amplitude. This process of the wavefront losing energy to the interior of the basin by long Poincaré waves continues throughout the evolution. At subsequent times, the resulting wave field is best described as a nearly basin-scale wavefront followed by an undular tail, with the wavelength decreasing towards the rear of the tail.

In Fig. 3, the effects of nonlinearity play a key role in the evolution of the wave field. By $t = 7$ h, the initial disturbance has steepened up to a near shock. However, the formation of the shock is prevented by the dispersive terms in Eqs. (2)–(4). When nonlinear steepening and dispersion are in balance, a collection of high-frequency solitary-like waves can be observed in the wave field; however, this is difficult to discern in Fig. 3. When the flow is animated, it appears that two-dimensional interactions between the solitary-like waves occur, and that the waves lose energy by interacting with the interior of the basin. As in the linear case (Fig. 2), the elevation at the front of the wave eventually decays sufficiently so that the elevated region behind the interfacial depression becomes the region of largest amplitude in the basin. After sufficient time has passed, solitary-like waves can be found in this secondary region of elevation due to nonlinear steepening, and the process continues with a further loss of energy downstream.

A more detailed look at the early time nonlinear evolution for the case when $\eta_0^{\max} = 0.25H$ is shown in Fig. 4. Fig. 4(a) reveals the key role that dispersion plays in the early evolution of the wave field: disallowing a shock in favour of a train of dispersive shortwaves and a coherent solitary-like wave. At later times, the primary wavefront is seen losing energy to its tail wave (of elevation). This effect was observed by Stastna et al. [25] and Helfrich [26] in simulations of the evolution of solitary waves affected by rotation. A comparison of panels (a) and (b) reveals decay in amplitude of the wave as

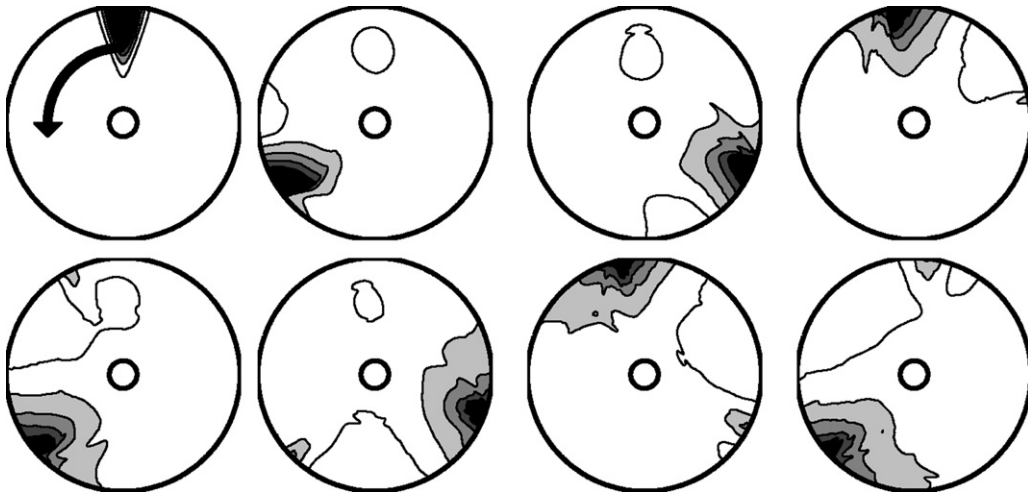


Fig. 5. Like Fig. 2, but with $\eta_0^{\max} = 0.25H$ and $f = 1.4544 \times 10^{-4} \text{ s}^{-1}$.

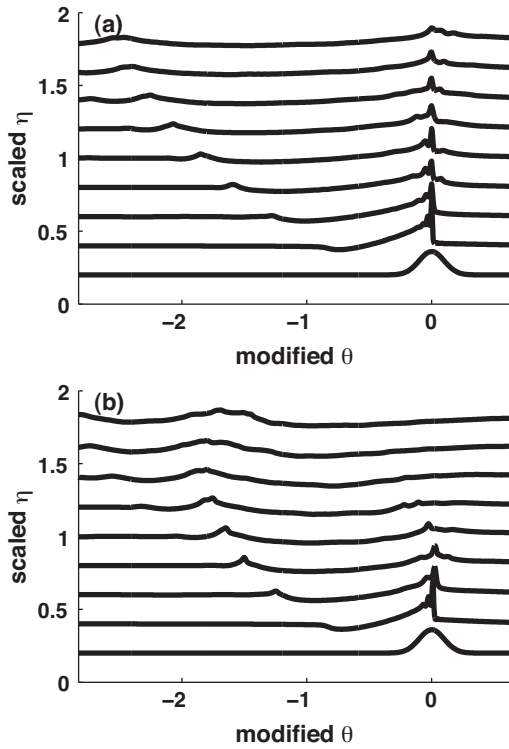


Fig. 6. 1D slices of the snapshots presented in Fig 5 (panel (a)) and 3 (panel (b)) at $r = r_{\max} = 8435$ m. In each panel, a single curve corresponds to a time in Fig. 3, with the lowest curve giving a slice through the initial condition ($t = 0$ h) and the uppermost curve giving a slice through the final snapshot ($t = 49$ h). The slices have been shifted in such a way that the main wave-front is centered about $\theta = 0$, and η has been made dimensionless by dividing by the undisturbed layer thickness H .

we move inwards from the coast ($r = r_{\max}$). Also visible is the fact that the portion of the wave in the interior of the basin leads the portion at the edge, due to the boundary curvature's influence on the portion of the wave nearest to the coast.

We now turn our attention to the effects of f -plane rotation on the evolution of the wave-field for an initial interfacial perturbation of fixed amplitude. In Fig. 5, f is almost doubled to $1.4544 \times 10^{-4} \text{ s}^{-1}$, reflecting the Coriolis frequency at the North Pole, the highest value of f possible on Earth. In this case, the Rossby deformation radius is

$L_D = 3852$ m, or about half-way between the inner and outer basin radii.

Due to the linear analysis performed by Stocker and Imberger [18], we expect increasing f to result in the strengthening of the linear Kelvin mode, thereby weakening the interactions between our coastally propagating disturbance and the interior of the basin. Indeed, this effect is expressed in our results in two main observations: firstly, it is found that the length of time required for the primary wavefront to lose energy to its tail is increased substantially when compared to Fig. 3; and secondly, the outward spreading of the initial disturbance to near basin scales takes considerably longer. Both of these effects are attributable to the relative strengthening of the Kelvin mode compared to the corresponding free Poincaré modes predicted by linear theory. This result may also be interpreted in terms of the Rossby deformation radius, L_D : a smaller value of L_D lowers the effect of boundary curvature, leading to a scenario more akin to a Kelvin wave propagating along a straight coastline, hence there are fewer radiating Poincaré waves. These effects can be visualized more clearly by directly comparing slices of the wave field at fixed times between the two simulations corresponding to $f = 1.4544 \times 10^{-4} \text{ s}^{-1}$ and $f = 7.8828 \times 10^{-5} \text{ s}^{-1}$ with $\eta_0^{\max} = 0.25H$. This comparison is done in Fig. 6. It can be seen that the simulation with the higher rotation rate maintains a coherent leading wave for twice as long as the lower rotation rate case. Furthermore, the steepening of the secondary wave is decreased in the high f case. Finally, in the high f case significantly more short wave activity upstream of the leading disturbance is evident (especially for the final three times shown).

3.4. Test Case III: the wave formation and propagation from an internal Kelvin-seiche and the influence of bottom bathymetry (hereafter, IKS)

In the final test case, we consider the evolution of an initially at rest, basin wide linear tilt in the density interface. The corresponding initial conditions for a west–east tilt are:

$$\eta_0 = \frac{ax}{r_{\max}}, \quad (28)$$

$$u_{\theta,0} = 0, \quad (29)$$

$$u_{r,0} = 0, \quad (30)$$

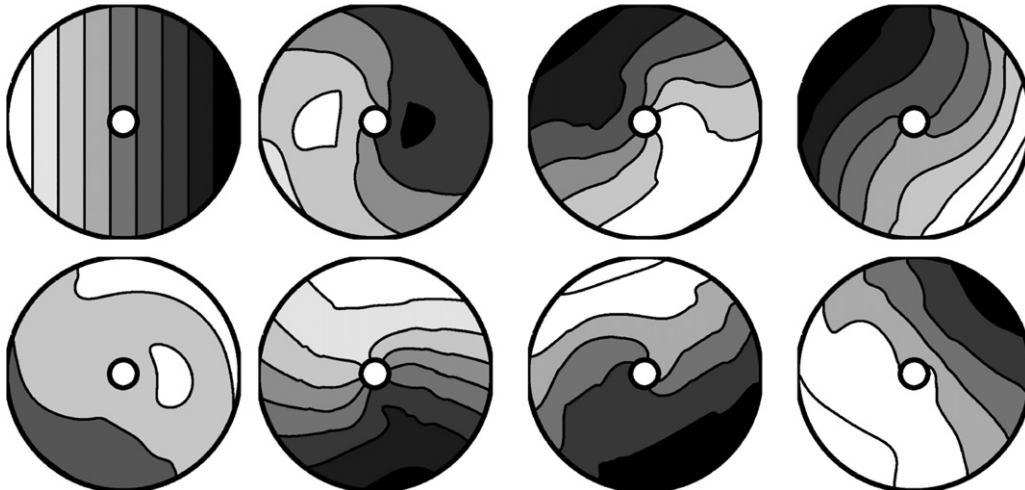


Fig. 7. Selected snapshots of the η field in the IKS test-case with $a = 0.1H$ at times $t = 0, 2.67, 5.33, 8.00$ h (top) and $t = 10.67, 13.33, 16.00, 18.67$ h (bottom). The contour interval is given by ten evenly spaced contours between $\eta = \eta_0^{\min} = -0.1H$ (white) and $\eta = \eta_0^{\max} = 0.1H$ (black).

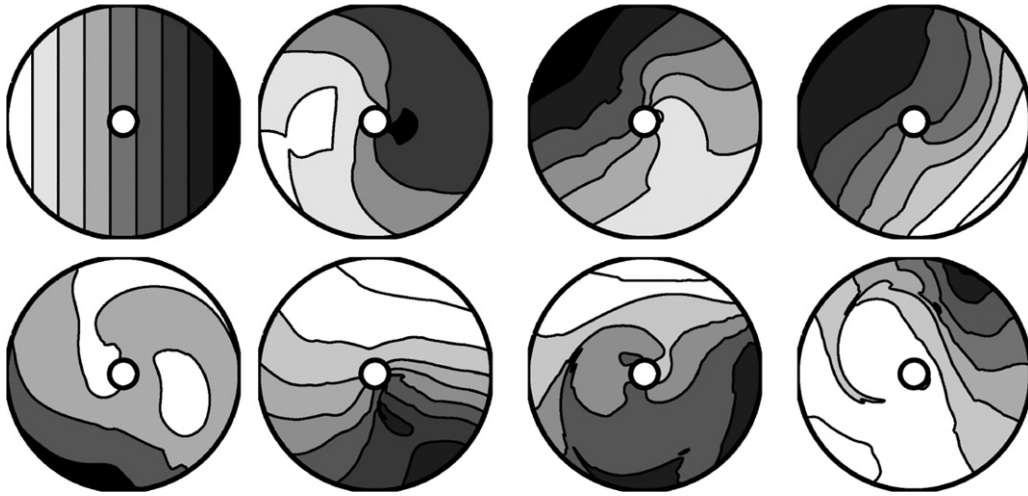


Fig. 8. Like Fig. 7, but with $a = 0.25H$.

where a is the maximum amplitude of the tilt. The physical parameters ($f, g, H, r_{max}, r_{min}$) are given by the same values used in Test Case II, intended to mimick the real-world situation of Lake Kinneret under summer stratification conditions.

In the case where $f = 0$ (no rotation), one would expect a single basin-scale periodic standing wave (or seiche) to result [2]. However, in the present case where $f = 7.8828 \times 10^{-5} \text{ s}^{-1} > 0$ (Northern Hemisphere), we expect the ensuing basin-scale dynamics to be driven by the lowest frequency rotating gravity mode from the linear theory, i.e., the Kelvin mode [18]. The ensuing cyclonic motion is typically referred to as a “Kelvin-seiche” [27].

Snapshots of this Kelvin-seiche motion at fixed times are shown in Figs. 7 and 8 corresponding to initial tilt amplitudes of $a = 0.1H$ and $a = 0.25H$, respectively. A comparison of the two figures reveals the effect of nonlinearity due to an increase in initial tilt-amplitude. In Fig. 8, the effects of nonlinear steepening are visible as the clustering of η -contours at later times and the emergence of long “filament waves” stretching across the basin (particularly at $t = 10.67 \text{ h}$ and $t = 18.67 \text{ h}$). As in Test Case II, the formation of shocks does not occur due to the dispersive nature of the model equations (the same dispersive effects would preclude shock formation in an actual lake).

Some information about the effect of nonlinearity, and the details of the wave field can be obtained from the line plots shown in Fig. 9. It can be seen that strongly non-sinusoidal waveform shapes occur in the larger amplitude case (panels (a) and (c)), with some short wave generation at later times. In contrast, the smaller amplitude case is nearly sinusoidal, for the times shown.

The final simulation shown here in Fig. 10(a) is intended to illustrate the numerical model’s robustness in dealing with situations where the bottom of the basin is not flat. Here, the depth profile was taken to be

$$H = \bar{H} \left(1 - \frac{1}{4} \left(\frac{r}{r_{max}} \right)^2 \right), \quad (31)$$

where $\bar{H} = 12.8 \text{ m}$. This profile reflects a lake with a bowl-shaped bottom topography and is a reasonable idealization for the large scale bathymetry of typical, real-world, mid-sized lakes. The effects of bottom topography are best observed by comparing the run that includes topography (Fig. 10(a)) to the same run but with a flat bottom (Fig. 10(b)). We compare these two runs at later times when considerable differences in the wave fields have had time to develop. Since the two depth profiles are similar near the interior of the basin and most different at the edge of the basin, a

primary difference between panels (a) and (b) in Fig. 10 is in the position of the main wave front. With the parabolic bottom topography, the long internal wave speed $\sqrt{g'H(x,y)}$ is lower near the edge of the basin than in the interior (essentially a WKB approximation due to the gradual change of depth), therefore we expect the near-edge wave front to travel more slowly than in the flat bottom case. Furthermore, a close comparison of the nonlinear “filament” waves (Fig. 10(c) and (d)) that radiate towards the interior of the basin from the primary wave front reveals that these waves undergo wave refraction as they cross depth isolines. This effect is

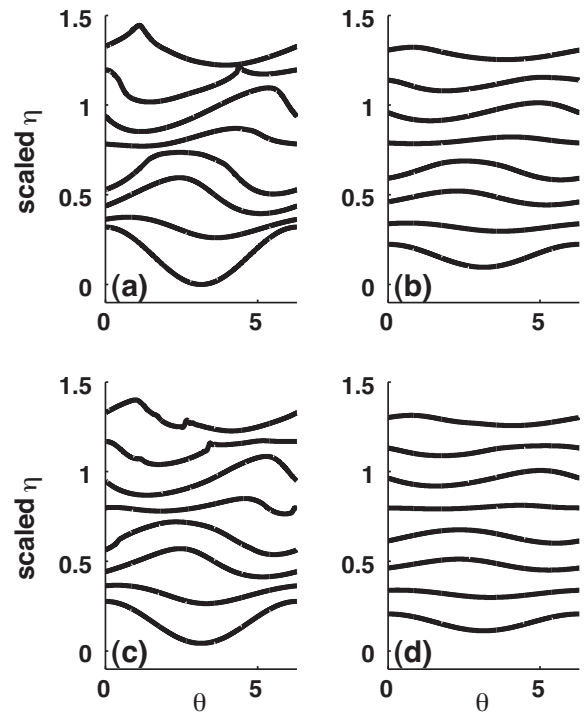


Fig. 9. Scaled η at $r = r_{max} = 8435 \text{ m}$ (panels (a) and (b)) and $r = 6167 \text{ m}$ (panels (c) and (d)) versus θ corresponding to Fig. 8 (panels (a) and (c)) and Fig. 7 (panels (b) and (d)). In each panel, the bottom-most profile corresponds to the initial conditions ($t = 0$) while the top-most profile corresponds to the bottom rightmost panel in Figs. 8 and 7 ($t = 18.67 \text{ h}$). The interfacial displacement η has been made dimensionless by dividing by the undisturbed layer thickness H .

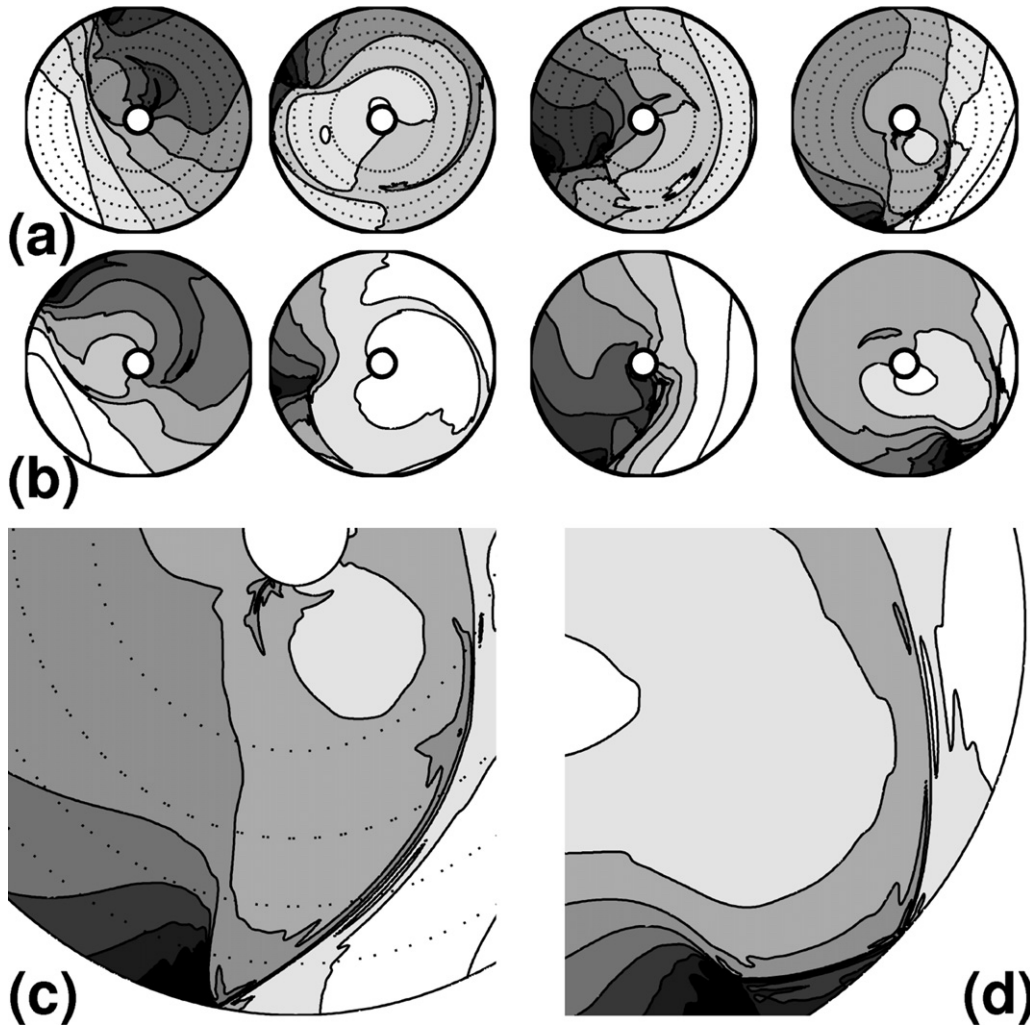


Fig. 10. (a) Selected snapshots of the η field in the IKS test-case with parabolic bathymetry and $\eta_0^{\max} = 0.25H_{\max}$ at times $t = 22.84, 25.53, 28.22, 30.91$ h. The contour interval is given by ten evenly spaced contours between $\eta = \eta_0^{\min} = -0.25H_{\max}$ (white) and $\eta = \eta_0^{\max} = 0.25H_{\max}$ (black). Four (dotted) depth contours are super-imposed on the plot, to indicate the shape of the bathymetry. (b) The same snapshots as (a) but without topography, i.e., the same run as Fig. 8 but at later times. Panels (c) and (d) show a magnified comparison between the with-topography and no-topography runs at $t = 30.91$ h.

also expected, since these waves are essentially propagating from a slow medium to a fast one (from the edge of the lake to the interior).

4. Summary/conclusions

A pseudospectral numerical method has been presented for solving a weakly non-hydrostatic (Boussinesq-type) rotating shallow water system in annular domains. The methodology employs a Fourier pseudospectral spatial discretization in the azimuthal direction and a Chebyshev pseudospectral spatial discretization in the radial direction after the model equations have been transformed to polar coordinates (r, θ) . The main benefit of using a pseudospectral spatial discretization technique is the lack of inherent dissipation that one frequently encounters in finite volume [6] or finite difference models. In the case of pseudospectral methods, the modeller must prescribe a small amount of artificial dissipation to stabilize the scheme, typically with spectral filtering, as was done in this manuscript. The temporal discretization method results in an elliptic pressure-type problem that must be solved at each time step. Due to the fact that the linear system resulting from the spatial discretization of this elliptic problem is ill-conditioned, large and dense (as is typical with pseudospectral spatial discretizations), direct solution methods are not possible,

and an approach using GMRES (Krylov-subspace) iterations with pre-conditioning was proposed. The pre-conditioner was taken to be the second-order central differences approximation to the elliptic operator. Since finite differences yield sparse matrix discretizations, the direct approach of calculating the LU-factorization of the pre-conditioning operator for re-use during GMRES iterations was available and employed.

The model was shown to be useful in performing simulations of internal wave dynamics in mid-sized lakes during the ice-free seasons when lakes are expected to possess a thermal stratification and (depending on their size) be affected by the Earth's rotation. The robustness of the numerical model was illustrated by considering different wave dynamical situations corresponding to different sets of initial conditions while varying the physical parameters of the equations over a wide range of physically relevant choices. These parameter choices included: (1) the strength of nonlinearity, i.e., extent of wave steepening, (2) the strength of the Coriolis force, i.e., the angular frequency of the rotating frame of reference, and (3) the bottom topography of the circular lake.

The results of the simulations shown in this manuscript appeared to agree well with intuition, well-known observations of wave dynamics in lakes and experiments [6,9,27], as well as past numerical simulations [11,25,26] and mathematical theory

[18] of internal waves. The main focus of our simulations was on the transfer of energy from large- (or basin-scale) waves to small-scale features such as dispersive wavetrains and high-frequency solitary-like waves. This agreement with previous results in the literature suggests that the model presented here may well prove useful in practical physical limnology applications. In particular, the lack of inherent numerical dissipation allows for the construction of a set of rational hypotheses regarding the behaviour of waves in mid-sized lakes that can be subsequently tested against field data.

Several possible improvements and extensions of the work presented above are possible. Possible improvements to the existing numerical methodology include: (1) using a time discretization scheme with higher order accuracy than the Leapfrog method used here, (2) adaptively tuning the filtering parameters to minimize the amount of numerical dissipation, and (3) using a modified Chebyshev grid in the radial direction that is not heavily clustered near $r=0$ to allow for larger time-steps. One possible extension to the model would extend the numerical solution procedure to a two-layer dispersive shallow water model (e.g., [6,7]) which would serve as a more realistic model for internal waves when compared to the single-layer, reduced-gravity model used here. A second important extension would be to solve either the Boussinesq-type equations (1)–(4), or a multi-layer extension of them, with an unstructured grid method to allow for simulations of the complex geometry of real-world lakes. Since the system of equations is, at least in part, a hyperbolic system of equations, a natural choice for such a spatial discretization is the discontinuous Galerkin finite element (DG-FEM) method that is often used to solve hyperbolic problems on unstructured triangular meshes as a high-order extension of the finite volume method [13].

Acknowledgments

This work was supported by the Natural Sciences and Engineering Research Council of Canada and the Shared Hierarchical Academic Research Network (SHARCNET). Early discussions with Christopher Subich regarding numerical linear algebra are gratefully acknowledged. We would also like to thank the two anonymous reviewers whose helpful suggestions and feedback helped to improve the manuscript.

References

- [1] J. Boussinesq, Théorie des ondes et des remous qui se propagent le long d'un canal rectangulaire horizontal, en communiquant au liquide contenu dans ce canal des vitesses sensiblement pareilles de la surface au fond, *Journal de Mathématique Pures et Appliquée, Deuxième Série* 17 (1872) 55–108.
- [2] A. Gill, *Atmosphere–Ocean Dynamics*, 1st ed., Academic Press, 1982.
- [3] S. Bunya, E. Kubatko, J. Westerink, C. Dawson, A wetting and drying treatment for the Runge–Kutta discontinuous Galerkin solution to the shallow water equations, *Comput. Methods Appl. Mech. Eng.* 198 (2009) 1548–1562.
- [4] P. Lynett, P.L.-F. Liu, A two-layer approach to wave modelling, *Proc. R. Soc. Lond. A* 460 (2004) 2637–2669.
- [5] C. Mirabito, C. Dawson, E. Kubatko, J. Westerink, S. Bunya, Implementation of a discontinuous Galerkin morphological model on two-dimensional unstructured meshes, *Comput. Methods Appl. Mech. Eng.* 200 (2011) 189–207.
- [6] A. de la Fuente, K. Shimizu, J. Imberger, Y. Niño, The evolution of internal waves in a rotating, stratified, circular basin and the influence of weakly nonlinear and nonhydrostatic accelerations, *Limnol. Oceanogr.* 53 (6) (2008) 2738–2748.
- [7] C.J. Cotter, D.D. Holm, J.R. Percival, The square root depth wave equations, *Proc. R. Soc. A* 466 (2010) 3621–3633.
- [8] P. Davidson, *Turbulence: An Introduction for Scientists and Engineers*, 1st ed., Oxford University Press, 2005.
- [9] A. Wuest, A. Lorke, Small-scale hydrodynamics in lakes, *Annu. Rev. Fluid Mech.* 35 (2003) 373–412.
- [10] G. Tomasson, W. Melville, Geostrophic adjustment in a channel: nonlinear and dispersive effects, *J. Fluid Mech.* 241 (1992) 23–48.
- [11] P. Brandt, A. Rubino, W. Alpers, J. Backhaus, Internal waves in the strait of messina studied by a numerical model and synthetic aperture radar images from ERS 1/2 satellites, *J. Phys. Oceanogr.* 27 (1997) 648–663.

- [12] R. Leveque, *Finite Volume Methods for Hyperbolic Problems*, Cambridge University Press, 2002.
- [13] J. Hesthaven, T. Warburton, *Nodal Discontinuous Galerkin Methods*, Springer, 2008.
- [14] J. Boyd, *Chebyshev and Fourier Spectral Methods*, 2nd ed., Dover Publications, 2001.
- [15] L. Trefethen, *Spectral Methods in MATLAB*, Society for Industrial and Applied Mathematics, 2000.
- [16] D. Durran, *Numerical Methods for Fluid Dynamics*, 2nd ed., Springer, 2010.
- [17] W. Thomson (Lord Kelvin), On gravitational oscillations of rotating water, *Proc. Roy. Soc. Edinburgh* 10 (1879) 92–100.
- [18] R. Stocker, J. Imberger, Energy partitioning and horizontal dispersion in a stratified rotating lake, *J. Phys. Oceanogr.* 33 (2003) 512–529.
- [19] C. Eskilsson, S. Sherwin, Spectral/hp discontinuous Galerkin methods for modelling 2D Boussinesq equations, *J. Sci. Comp.* 22 (2005) 269–288.
- [20] J.P. Boyd, F. Yu, Comparing seven spectral methods for interpolation and for solving the Poisson equation in a disk: Zernike polynomials, Logan–Shepp ridge polynomials, Chebyshev–Fourier series, cylindrical Robert functions, Bessel–Fourier expansions, square-to-disk conformal mapping and radial basis functions, *J. Comput. Phys.* 230 (4) (2011) 1408–1438.
- [21] R. Peyret, *Spectral Methods for Incompressible Viscous Flow*, Springer-Verlag New York, Inc, 2002.
- [22] A. Iserles, *A First Course in the Numerical Analysis of Differential Equations*, Cambridge University Press, 1996.
- [23] L. Trefethen, D. Bau, *Numerical Linear Algebra*, Society for Industrial and Applied Mathematics, 1997.
- [24] A. Saggio, J. Imberger, Internal wave weather in a stratified lake, *Limnol. Oceanogr.* 43 (2001) 1780–1795.
- [25] M. Stastna, F. Poulin, K. Rowe, C. Subich, On fully nonlinear vertically trapped wave packets, *Phys. Fluids* 21 (2009) 106604.
- [26] K. Helfrich, Decay and return of internal solitary waves with rotation, *Phys. Fluids* 19 (2007) 026601.
- [27] U. Lemmin, C. Mortimer, E. Bauerle, Internal seiche dynamics in Lake Geneva, *Limnol. Oceanogr.* 501 (1) (2005) 207–216.



Derek Steinmoeller is a recent graduate of the M.Math program in the department of Applied Math at the University of Waterloo. His master's thesis was on numerical methods for solving equations governing large-scale ocean circulation. Now in the Ph.D. program at Waterloo, Derek works with Marek Stastna and Kevin Lamb on applying novel high-order numerical methods for solving model equations governing internal wave dynamics in mid-sized lakes with both simple and complex geometries to help better understand the bio-geochemical processes in these lakes.



Marek Stastna studies two related problems. The first involves computer models of climate changes that took place near the end of the last Ice Age when large lakes that covered the Canadian Prairies suddenly drained into the North Atlantic and Arctic oceans. This influx of freshwater disrupted the system of ocean currents that moves heat northward and maintains a temperate climate in Europe. By comparing computer simulations with the geological record Marek and his collaborators aim to improve our understanding of possible changes in the future climate. Second, Marek looks at the small scale fluid dynamics, or nuts and bolts, of the first problem. These studies, again using computer models, examine eddies in the coastal oceans and large waves in the interior of the ocean, and aim to improve both the large-scale climate models themselves and the interpretations scientists make of the results they produce (UW Math, Annual Report 2004).



Kevin's work helps biologists understand how nutrients, oxygen and organisms mix and move in water to affect plant and animal life. It helps environmental agencies assess the impact of global warming. And it helps oceanographers to better understand the sea. Kevin's primary area of research is on nonlinear internal ocean waves. Internal waves occur in density-stratified fluids. In the ocean the stratification results from variable temperature and salinity. Waves are generated primarily by tidal flow over topography and by winds. Kevin's goal is to better understand the wave generation process and the effect of waves on the environment through high-resolution simulations using fully nonlinear, non-hydrostatic numerical models. These simulations help Kevin analyze the behaviour of internal waves and wave-induced mixing. Kevin is a member of the Environmental and Geophysical Fluid Dynamics research group (UW Math, Annual Report 2005).